

High-energy emissions from the gamma-ray binary 1FGL J1018.6-5856

A. M. Chen^{1,2}, C. W. Ng², J. Takata³, Y. W. Yu¹,

and

K. S. Cheng²

chensm@mails.ccnu.edu.cn; hrspksc@hku.hk

ABSTRACT

The gamma-ray binary 1FGL J1018.6-5856 is known to be composed of a massive star with a compact object with an orbital period of 16.54 days. We study mechanisms of high-energy emissions (X-ray, GeV, and TeV γ -rays) from this binary system. The paper is composed of two parts. In the first part, we re-analyze the GeV emission from 1FGL J1018.6-5856 using 7 yrs of the observational data of *Fermi*/LAT. The data analysis of phase-resolved spectrum suggests that the 0.1-10 GeV emissions may contain two different components: (1) a simple power-law with exponential cutoff component in the LOW state; (2) an additional component extended to ~ 10 GeV in the HIGH state. In the second part, we develop a model to explain the multi-wavelength emissions of this binary. Assuming that 1FGL J1018.6-5856 includes a pulsar, the GeV spectrum in the LOW state can be well explained by the two-layer outer gap model of pulsar magnetosphere. As the pulsar is orbiting around the star, the pulsar is considered to be wrapped by two kinds of termination shock: a bow shock due to the interaction between pulsar wind and stellar wind, and a back shock due to the effect of orbital motion. We proposed that X-rays are mainly produced by the synchrotron radiation at the apex of the bow shock, and TeV γ -rays are mainly produced by the inverse-Compton scattering at the back shock. The sharp peak in X-ray and TeV light curves are produced by in the shock tail due to the Doppler boosting effect at inferior-conjunction while another broad sinusoidal modulations are possibly produced by the apex of the bow shock and the back shock due to variations of shock conditions.

¹Institute of Astrophysics, Central China Normal University, Wuhan 430079, China

²Department of Physics, The University of Hong Kong, Pokfulam Road, Hong Kong

³School of physics, Huazhong University of Science and Technology, Wuhan 430074, China

Subject headings: binaries: close — gamma rays: stars — X-rays: binaries —
 raiation mechanisms: non-thermal

1. Introduction

The gamma-ray binary is a class of high-mass X-ray binary systems containing a compact object and a massive star and emit high-energy γ -rays beyond 1MeV (see Dubus 2013 for a review). The compact object is widely thought to be a rotation-powered pulsar, although it still remains to be proven for most binary systems. Until now, 7 high-mass gamma-ray binaries have been detected, namely, PSR B1259-63/LS2883 (Aharonian et al. 2005), LS 5039 (Aharonian et al. 2006), LS I+61°303 (Albert et al. 2006), H.E.S.S. J0632+057 (Hinton et al. 2009), 1FGL J1018.6-5856 (Ackermann et al. 2012), PSR J2032+4127/MT91 213¹ (Lyne et al. 2015) and LMC P3 (Corbet et al. 2016, the first gamma-ray binary to be found outside the Milky Way). Only PSR B1259-63/LS 2883 and PSR J2032+4127/MT91 213 have been confirmed to contain a pulsar so far.

The γ -ray source 1FGL J1018.6-5856 (J1018.6 hereafter for short) was identified as a gamma-ray binary by Ackermann et al. (2012) based on the blind search for periodic sources of γ -ray data taken by *Fermi*/LAT. The follow-up observations in radio, optical and X-ray also confirmed the binary nature of this source with a period of 16.6 days. The optical spectroscopy indicates that the optical counterpart is a massive main-sequence star with a spectral type of O6V((f)). The distance derived from the interstellar absorption lines of the companion star is $d_L = 5 \pm 2$ kpc. Later Abramowski et al. (2012, 2015) also discover the TeV counterpart of this system using the *HESS* telescope. The TeV light curves show similar orbital modulations as seen in X-ray band. An et al. (2013, 2015) gave detail reports on *NuSTAR*, *XMM-Newton*, and *Swift-XRT* observations of J1018.6 and constrained the orbital period to be 16.544 ± 0.008 days. They found that the X-ray light curves have a regular spike with small variability and a broad sinusoidal modulation. The behavior of J1018.6 at different orbital phases is similar in X-ray, GeV, and TeV bands, showing in all cases a maximum flux near phase 0 ²(see Fig.3 in Abramowski et al. 2015 for the TeV, GeV and X-ray light curves of J1018.6). Strader et al (2015) presented medium-resolution optical spectroscopy of the O star secondary of J1018.6 using the SOAR telescope. They find that

¹Strictly speaking, PSR J2032+4127/MT91 213 is a pulsar/Be star binary system resemble to PSR B1259-63/LS2883, but its TeV counterpart is still not detected.

²The γ -ray maximum is denoted as phase 0 in Ackerman et al. (2012), and we use the same denotes in the paper.

the O star has a low radial velocity with semi-amplitude of 11-12 km · s⁻¹ which favors a neutron star primary. They also find that the high energy (X-ray and γ -ray) flux maxima occur when the star is behind the compact object along the line of sight.

Unfortunately, the orbital parameters and accurate conjunction phases of J1018.6 are still unknown yet, and only limited conclusions can be drawn on the relation between the compact object and the companion star (Abramowski et al. 2015). However, J1018.6 shares many properties with another well studied gamma-ray binary LS 5039. Both two binary systems are composed of an almost identical massive star (O6.5(f) for LS 5039, and O6V(f) for J1018.6) and a compact object orbiting on a timescale of days ($P_{\text{orb}} = 3.9$ days for LS 5039, and $P_{\text{orb}} = 16.5$ days for J1018.6). They are fairly steady γ -ray sources and their periodic modulations have not shown large changes (Ackerman et al. 2012). The spectrum of J1018.6 also resemble that of LS 5039 (i.e., a power-law in X-ray band and a power-law with exponential cut-off in GeV band). Both of them show a maximum flux when the star is behind the compact object in X-ray and TeV light curves. With the facts given above, we can give rough constraints on the system parameters and use the emission model which has been applied to LS 5039 (e.g., Takata et al. 2014) to explain the high energy emissions from J1018.6.

The multi-wavelength emissions of LS 5039 has been well studied under the pulsar model. In the rotation-powered pulsar scenario, the interactions between a pulsar wind and a stellar wind will form a bow shock (Tavani & Arons 1997; Dubus 2006a). The effect of the orbital motion of pulsar also produce a termination shock in the opposite direction of companion star (Bosch-Ramon et al. 2012; Zabalza et al. 2013; Takata et al. 2014). The shocks accelerate electrons and/or positrons from the pulsar wind, and then emit X-rays and TeV γ -rays through synchrotron radiation and inverse-Compton process, respectively. The emissions from the shocked regions are expected to show orbital variations due to a combination of the following effects: anisotropic inverse-Compton scattering, the γ -ray absorption, the Doppler-boosting effect, etc.

Besides the shock emissions, the pulsar itself will also contribute to the high energy emissions of the system in different ways (Sierpowska-Bartosik & Torres 2007; Kapala et al. 2010; Torres 2011; Takata et al. 2014). The first component is due to pulsed emission originating in outer-gaps of the pulsar which peaks around 1 GeV. This magnetospheric emission is not expected to vary along its orbit in a binary. Alternatively, the high-energy emission could also arise from the un-shocked pulsar wind via up-scattering of ambient photons provided by the companion star (Kirk, Ball & Skjaeraasen 1999; Cerutti, Dubus & Henri 2008). A narrow component appears at the high-energy spectra peaking at an energy $\gamma_w m_e c^2$ (in the Klein-Nishina regime), with γ_w being the Lorentz factor of the wind. This

modulated anisotropic inverse Compton emission is expected to peak when the star is in front of the pulsar along the line of sight, with a stronger effect for more edge-on inclinations.

This work purports to explain the high energy emissions from J1018.6 under the rotation-powered pulsar scenario mentioned above. The main purpose of this study are composed of two parts: (1) to present results of the observational analysis using 7 yr *Fermi*/LAT data, which provide us with more detailed information on the GeV emission from J1018.6, and (2) to develop an emission model to discuss the radiation processes of the X-ray, GeV, and TeV emissions. The paper is organized as follows: in Section 2, we report on the results of our analysis of the *Fermi*/LAT data. We describe the emission from the pulsar magnetosphere and shocked wind regions in Section 3 and Section 4. In Section 5 we compare the model predictions with the results of the multi-wavelength observations. Finally, a brief discussion and summary are given in Sections 6.

2. Data Analysis

We analyzed the gamma-ray orbital light curve of J1018.6 using the data from the *Fermi* Large Area Telescope. Photon events with energy ranged from 100 MeV to 100 GeV and time ranged from 2008-08-09 to 2015-08-08 were selected, from the “Pass 8 Source” event class with the corresponding instrumental response function of “P8R2_SOURCE_V6”. The region of interest (ROI) is a $20^\circ \times 20^\circ$ square centered at the epoch J2000 position of the source: (R.A., Dec) = ($10^{\text{h}}18^{\text{m}}55.18^{\text{s}}$, $-58^\circ56'44.2''$). To reduce the contamination from the Earth’s albedo, time intervals were excluded when the ROI is observed at a zenith angle greater than 90° . The *Fermi* Science Tools package version v10r0p5³ was used in the data analyses in this study. The *gtlike* tool was used to perform maximum binned likelihood analysis to obtain the spectral model for all the 3FGL catalog sources (*gll_psc_v16.fit*) (Acero et al. 2015) that are within 25° from the center of ROI, the galactic diffuse emission (*gll_iem_v06*) and the isotropic diffuse emission (*iso_P8R2_SOURCE_V6_v06*), available from the *Fermi* Science Support Center (FSSC)⁴. The spectral parameters for sources that are non-variable and located 5° away from the center are fixed to their catalog values. Four extended sources within the region: HESS J1303-631, Puppis A, Vela Jr and Vela X, were modeled by the extended source templates provided by the FSSC. With the spectral indices fixed to the global fit and leaving only the normalization parameters free, this model is then used to calculate the orbital light curve. The orbital phase is assigned to each of the photons using

³Available at <http://fermi.gsfc.nasa.gov/ssc/data/analysis/software/>

⁴<http://fermi.gsfc.nasa.gov/ssc/>

the TEMPO2 package (Hobbs et al. 2006) with the *Fermi* pulg-in (Ray et al. 2011). In the timing model, we assumed the orbital period to be 16.544 days (An et al. 2015) and the binary model to be a main-sequence/pulsar binary (Wex, 1998). The whole data set is then separated into 10 phase bins. Using the *gtlike* tool (binned likelihood analysis) and the model obtained in the global fit, we derived the energy flux of J1018.6 in each orbital phase (Fig. 1).

We performed spectral analysis in the selected orbital phase intervals to investigate if the spectrum of 1FGL J1018.6-5856 is varying throughout the orbital period. We defined the phase interval between 0.0 - 0.3 and 0.8 - 1.0 as the “HIGH” state and the interval between 0.3 - 0.8 as the “LOW” state. We used the same data set described above and sub-selected these two states. Also, we used the same spectral model as the initial guess. The spectral form of J1018.6 is modeled by a power-law with simple exponential cutoff:

$$\frac{dN}{dE} = N_0 \left(\frac{E}{E_0} \right)^{-\Gamma} \exp \left(-\frac{E}{E_C} \right), \quad (1)$$

where N_0 is the normalization constant, E_0 is the scale factor of energy, Γ is the spectral power-law index and E_C is the cut-off energy. Using binned likelihood analysis, the best-fit parameters for HIGH state are $N_0 = (1.20 \pm 0.02) \times 10^{-9}$, $\Gamma = -1.82 \pm 0.02$ and $E_C = 3000 \pm 190$. For LOW state, $N_0 = (1.19 \pm 0.03) \times 10^{-9}$, $\Gamma = -1.94 \pm 0.01$ and $E_C = 3277 \pm 175$. Then, we obtained the spectral points by performing the model fit in each energy band, using a simple power-law form for J1018.6:

$$\frac{dN}{dE} = N_0 \left(\frac{E}{E_0} \right)^{-\Gamma}, \quad (2)$$

where Γ is assumed to be -2.1 . Upper limit is derived when the detection significance is less than 3σ . The phase-resolved spectra are shown in Fig. 2.

3. Magnetospheric Emissions

The power-law with exponential cut-off spectrum in GeV band of J1018.6 is typical of the γ -ray pulsar observed by *Fermi*/LAT. It is indicated that the GeV emissions are mainly contributed by the pulsar magnetospheric radiations.

Currently, because there is no existing published result on the timing parameters of the pulsar in J1018.6, the properties of the pulsar remains unknown. Yet, in order to explain the complete emission spectrum of J1018.6, the magnetospheric contribution cannot be ignored. We used the standard outer gap model (Cheng et al. 1986a & 1986b) to simulate the

curvature spectrum from the charge accelerations in the outer gap, which extends from the null charge surface to the light cylinder. The separation of the oppositely charged particles induces an electric potential in the space between them, leading to the growth of the outer gap. On the other hand, the curvature photons can undergo photon-photon pair creation with the softer photons from the pulsar surface. The accumulation of charges will reduce the electric potential, resulting in the depletion of the outer gap. These two instantaneously occurring processes can be resembled by the two-layer structure (Wang et al. 2010 & 2011) which defines contrasting charge densities for the primary acceleration and the screening regions. In this study, we simulate the magnetospheric emission from a pulsar that has a magnetic inclination angle $\alpha = 40^\circ$ and a viewing angle at $\beta = 120^\circ$ (or 60°). The period and the surface magnetic field strength are assumed to be $P = 0.05$ s and $B = 10^{12}$ G respectively. The pulsar has an average charge density of 0.7 Goldreich-Julian charge density and the primary acceleration region occupies 70% of the gap thickness.

The observed gamma-ray magnetospheric spectrum of J1018.6 (LOW state in Fig. 2) is flat in the energy range below 1 GeV but at the same time has detection beyond 10 GeV. These features indicate that the pulsar could have an outer gap which gap size is varying in time. This is a result of the dynamical development of the local charge density and electric field strength, which depends on the instant pair creation rate and the current flow (Takata et al. 2016). When the gap size increases, the charges are accelerated by a greater electric potential, and thus the maximum energy of photon radiated can be higher, and vice versa. In the simulation, we simplify the dynamics by superposing the curvature spectrum of the pulsar in different gap fractions, together with a weighting factor that describes the fraction of time that the gap fraction remains at the corresponding value. A similar non-stationary superposition method has been used by Chai et al. (2016) to explain the sub-exponentiality in the cutoff spectrum for the Vela and Geminga pulsars. In their model, they assumed a power-law distribution of the curvature spectrum in different cutoff energies derived from the very fine phase-resolved spectrum and superpose the results to obtain the sub-exponential cutoff spectrum. In this study, we adopted a similar power-law relation between the gap fraction (f) and the fraction of time (w_f):

$$w_f = \frac{f^\lambda}{\sum f^\lambda}, \quad (3)$$

where λ is assumed to be -2.487 from fitting the resultant superposed spectrum to the *Fermi*-observed spectral energy distributions at the LOW state.

4. Shock emissions

The interactions between the pulsar wind and the stellar wind will form a bow shock with a hollow-like tail, and the effect of the orbital motion of pulsar will also produce a back shock in the opposite direction of companion star. The shocks accelerate the electrons and positrons of the pulsar wind, and then emit the X-rays and TeV γ -rays through synchrotron radiation and inverse-Compton process, respectively.

4.1. Orbital Phase

Considering an energetic pulsar in orbit around the massive companion star, the orbital separation d is given by (e.g., Dubus 2006b)

$$d = \frac{a(1 - e^2)}{1 + e \cos \theta}, \quad (4)$$

with the semi-major axis $a = (GMP_{\text{orb}}^2/4\pi^2)^{1/3}$, M the total binary mass, e the eccentricity, θ the true anomaly. The orbital phase (mean anomaly) is defined as

$$\phi = \frac{\varphi - e \sin \varphi}{2\pi} + \phi_0, \quad (5)$$

with the eccentric anomaly

$$\varphi = 2 \arctan \left(\sqrt{\frac{1-e}{1+e}} \tan \frac{\theta}{2} \right), \quad (6)$$

and ϕ_0 is the orbital phase at periastron which equals 0 for most cases.

The system parameters and orbital phases of J1018.6 are still unknown yet. However, J1018.6 shares many similarities with another well studied gamma-ray binary LS 5036, a limited conclusions can be drawn by comparing the properties between J1018.6 and LS 5039. The period of J1018.6 is about 4 times longer than LS 5039, which means that a semi-major axis is larger by a factor of 2.5 than in LS 5039. The low amplitude of the flux modulation can be interpreted as a sign of a low eccentricity orbit and low inclination. In our calculation, we adopted a modest value of $e \simeq 0.35$ and $i \simeq 40^\circ$ which is similar to the case of LS 5039. According to the optical spectroscopy analysis done by Strader et al (2005), finding that the high-energy flux maxima occur when the star is behind the compact object along the line of sight, we estimate the value of periastron angle with $\omega \simeq 90^\circ$. We illustrate the orbital phase of J1018.6 applied in our model in Fig. 3. We should point out that the accurate determination of system parameters and orbital phases still need further observations.

4.2. Shock Geometry

The location of the terminal bow shock is determined by the dynamical pressure balance between the pulsar wind and the stellar wind (Dubus 2006a):

$$\frac{L_{\text{sd}}}{4\pi r_s^2 c} = \rho_w v_w^2, \quad (7)$$

with $\rho_w = \dot{M}/4\pi R^2 v_w$ is the wind density. Then the distance from the shock contact discontinuity in the shock apex to the pulsar is determined by

$$r_s = d \frac{\eta^{1/2}}{1 + \eta^{1/2}}, \quad (8)$$

with $\eta = L_{\text{sd}}/c\dot{M}v_w$. L_{sd} is the spin down luminosity of the pulsar, c is the speed of light, \dot{M} is the mass loss rate of the massive star and v_w is the velocity of the stellar wind. We assume that the value of η is constant along the whole orbit.

Away from the apex, the shock surface becomes a hollow cone. The half opening angle of the shock contact discontinuity can be well described by (Eichler & Usov 1993)

$$\theta_{\text{shock}} = 2.1(1 - \bar{\eta}^{2/5}/4)\bar{\eta}^{1/3}, \quad (9)$$

where $\bar{\eta} = \min(\eta, \eta^{-1})$.

The effect of the orbital motion of pulsar will also produce a termination back shock in the opposite direction of companion star. The distance from the back shock to pulsar can be determined by the balance between the ram pressure of the stellar wind due to Coriolis force and the ram pressure of the pulsar (Bosch-Ramon & Barkov 2011):

$$\frac{L_{\text{sd}}}{4\pi x_s^2 c} = \rho_w (2\Omega x_s)^2, \quad (10)$$

with $\Omega = 2\pi/P_{\text{orb}}$ is the angular velocity of the binary system. Then the distance from the shock contact discontinuity in the shock apex to the pulsar is determined by (Bosch-Ramon & Barkov 2011; Zabalza et al. 2013):

$$x_s \sim \sqrt{\frac{L_{\text{sd}} v_w}{\dot{M} c (2\Omega)^2}}, \quad (11)$$

with $\Omega \sim 10^{-6}/s$ for J1018.6 yields $x_s \sim 2 - 4d$.

4.3. Shock Radiations

Although some gamma-ray binaries show correlated X-ray and TeV γ -ray flux variations in light curves, however, for J1018.6, it is difficult to model both X-ray and TeV γ -ray emissions using a one zone population of electrons. Furthermore, the phase-averaged TeV γ -ray spectrum of J1018.6 extends up to $\sim 20\text{TeV}$ with $E_{\text{break}} \geq 10\text{TeV}$, posing constraints on the magnetic field with $0.001 \leq B \leq 0.1\text{G}$, with such a low magnetic field can not explain the observed X-ray flux level (Abramowski et al 2015). A similar situation also appears in the case of LS 5039. Therefore, with the facts given above point toward to the presence of at least two particle populations or two radiation zones to explain the X-ray and TeV γ -ray emission. In this paper, we use a similar emission model proposed by Takata et al. (2014): we assumed that the X-ray emissions are mainly produced by the apex region of the bow shock due to a higher magnetic field and the TeV γ -rays are mainly produced by the back shock with a lower magnetic field and small absorption. The intense stellar photon field at the shock apex, and corresponding high opacities owing to pair production will reduce the TeV emissions at this region greatly. The synchrotron radiation from the back shock can be ignored because the magnetic field is small compare to the shock apex. In our calculations, we approximate that the observed emissions are mainly produced in three regions: the bow shock (with apex and tail), and the back shock as illustrated in Fig. 4. The radiation in the shock apex and the back shock are isotropic since the bulk motion is non-relativistic. As the particle flow propagating away from the shock apex, the bulk Lorentz will increase gradually to relativistic in the shock tail (Bogovalov et al. 2008, 2012). So the emissions from the shock tail should be beamed. When the line of sight is near the beaming direction, we will receive the Doppler-boosted radiations (e.g., Kong et al. 2012). The sharp peaks around phase 0 in X-ray and TeV light curves can be produced by the Doppler boosting effect in the tail of the bow shock.

4.3.1. Magnetic Field

In the free pulsar wind region, the magnetic energy will be gradually converted into the particle energy from the light cylinder to the terminal shock. We assume that the variation of the magnetization of pulsar wind σ follows a simple power-law form (e.g., Kong et al. 2011, 2012)

$$\sigma = \sigma_{\text{L}} \left(\frac{r}{r_{\text{L}}} \right)^{-\alpha}, \quad (12)$$

with σ_{L} being the magnetization at the light cylinder r_{L} . According to the standard pulsar wind theory, the laboratory frame magnetic field B_{p} at r_{s} of pre-shocked region is given by

(Kennel & Coroniti 1984a,b):

$$\frac{B_p^2}{4\pi} \left(\frac{1 + \sigma}{\sigma} \right) = \frac{L_{sd}}{4\pi r_s^2 c}. \quad (13)$$

Then the downstream magnetic field for $\sigma \ll 1$ at shock region can be calculated using perpendicular MHD shock jump conditions (Kennel & Coroniti 1984a,b; Dubus et al. 2015)

$$B = \frac{1}{\hat{\gamma} - 1} \left[\frac{L_{sd}}{r_s^2 c} \left(\frac{\sigma}{1 + \sigma} \right) \right]^{1/2}, \quad (14)$$

with $\hat{\gamma} = 4/3$ is the adiabatic index of the flow. We can estimate the magnetic field at the shock regions using the equations above: with $\sigma(r_s) \sim 0.1$ and $\sigma(x_s) \sim 0.008$, we have $B(r_s) \sim 5\text{G}$ and $B(x_s) \sim 0.2\text{G}$ for the bow shock and the back shock region, respectively.

4.3.2. Electron Distribution

It is usually assumed that the electrons in the shocked pulsar wind can be accelerated to a power-law distribution:

$$Q(\gamma_e) = K \gamma_e^{-p} \quad \text{with} \quad \gamma_{e,\min} \leq \gamma_e \leq \gamma_{e,\max}, \quad (15)$$

and K is the normalization of particle distribution at the shock. The minimum Lorentz factor of the shocked pulsar wind is assumed to be the average Lorentz factor of cold pulsar wind at terminal shock with $\gamma_{e,\min} \approx \gamma_w$. The maximum Lorentz factor is determined by the balance between the accelerate timescale $\tau_{\text{acc}} = 2\pi\zeta R_L/c$ and the synchrotron loss timescale $\tau_{\text{syn}} = \gamma_e m_e c^2 / P_{\text{syn}}$, so $\gamma_{e,\max} = (3e/\zeta\sigma_T B)^{1/2}$. The electron numbers can be calculated from

$$\dot{N} = \frac{\Delta\Omega}{4\pi} \frac{L_{sd}}{\gamma_w(1 + \sigma)m_e c^2}, \quad (16)$$

with $\Delta\Omega/4\pi$ is the fraction of pulsar wind electrons injected into the shock front⁵.

The electrons will lose their energies through radiative cooling or adiabatic cooling processes. The evolved spectrum can be obtained from the continuity equation of the electron distribution (Ginzburg & Syrovatshii 1964):

$$\frac{\partial n(\gamma_e, t)}{\partial t} + \frac{\partial \dot{\gamma}_e n(\gamma_e, t)}{\partial \gamma_e} = Q(\gamma_e), \quad (17)$$

⁵Strictly speaking, the power in injected electrons is a fraction of the spin-down luminosity $L_{\text{inj}} \simeq \epsilon L_{\text{sd}}$. We leave the uncertain coefficient in $\Delta\Omega/4\pi$.

where $\dot{\gamma}_e$ is the total energy loss rate of the electrons and $Q(\gamma_e)$ is the injection rate. Assuming $\partial n(\gamma_e, t)/\partial t = 0$, the spectrum at a steady state can be acquired:

$$n(\gamma_e) = \frac{1}{|\dot{\gamma}_e|} \int_{\gamma_e}^{\gamma_{e,\max}} Q(\gamma'_e) d\gamma'_e. \quad (18)$$

For a steady-state, non-thermal source where electrons are rapidly cooling by emitting synchrotron radiation and inverse-Compton scattering, the total energy loss rate of the electrons is (Moderski et al. 2005)

$$\dot{\gamma}_e = \dot{\gamma}_{\text{syn}} + \dot{\gamma}_{\text{IC}} = \frac{4c\sigma_{\text{T}}u_{\text{B}}}{3m_e c^2} \gamma_e^2 (1 + qF_{\text{KN}}), \quad (19)$$

where $q = u_{\star}/u_{\text{B}}$, with $u_{\text{B}} = B^2/8\pi$ being the magnetic energy density, $u_{\star} = L_{\text{star}}/4\pi cR^2$ being the seed photon energy density. For a Planckian (black-body) distributed seed photons from the companion star can be well approximated as a mono-energetic photon distribution with energy $\epsilon_0 = 2.8kT_{\star}$. So $F_{\text{KN}} \simeq (1 + b)^{-1.5}$ and $b = 4\gamma_e(2.8kT_{\star}/m_e c^2)$ (Moderski et al. 2005). The radiative cooling timescale τ_c for an electron with Lorentz factor γ_e is

$$\tau_c(\gamma_e) = \frac{3m_e c}{4\sigma_{\text{T}}\gamma_e u_{\text{B}}} / (1 + qF_{\text{KN}}). \quad (20)$$

For a source with the dynamical timescale τ_{dyn} , the electron number at a given Lorentz factor that can accumulate in the source could be simply calculated by (Moderski et al. 2005; Kong et al. 2012)

$$N(\gamma_e) \simeq \dot{N}Q(\gamma_e) \min[\tau_c(\gamma_e), \tau_{\text{dyn}}], \quad (21)$$

with $\tau_{\text{dyn}} = 3r_s/c$ is the typical dynamical timescale for the post-shock of γ -ray binary.

In Fig. 5, we show the cooling timescales of electrons in the bow shock and the back shock. We can see that the radiative loss timescales are much shorter than the dynamical timescales of the flow in the bow shock region. The the radiative cooling of electrons with $\gamma_e < \gamma_{\text{KN}} = m_e c^2/4\epsilon_0$ and $\gamma_{\text{KN}} < \gamma_e < \gamma_s = \gamma_{\text{KN}}(q^{2/3} - 1)$ are mainly dominated by the inverse-Compton process in the Thomson regime and Klein-Nishina regime, respectively. At higher energies, the Compton rate decreases due to the KN effects and eventually synchrotron cooling always dominated for $\gamma_e > \gamma_s$. The IC spectra have high-energy break at $h\nu(\gamma_s)$ caused by the rapidly cooling of synchrotron radiation. The value of γ_s is very sensitive to the strength of magnetic field, which means that the strength of magnetic field in the shock regions will have a strong impact on the TeV spectrum.

4.3.3. Radiation process

The synchrotron radiation power at frequency ν from a single electron with Lorentz factor γ_e is given by (Rybicki & Lightman 1979)

$$P_\nu^{\text{SYN}}(\gamma_e) = \frac{\sqrt{3}e^3B}{m_e c^2} F\left(\frac{\nu}{\nu_c}\right), \quad (22)$$

where $\nu_c = 3\gamma_e^2 eB/(4\pi m_e c)$. The function $F(x)$ is defined as

$$F(x) = x \int_x^{+\infty} K_{5/3}(k) dk, \quad (23)$$

with $K_{5/3}$ being the modified Bessel function of order of 5/3.

The external inverse-Compton radiation power at frequency ν from a single electron with Lorentz factor γ_e is given by (Aharonian & Atoyan 1981)

$$\frac{dP_\nu^{\text{EIC}}(\gamma_e)}{d\Omega} = \frac{3\sigma_T}{4\pi} \int_{\nu_s, \min}^{\infty} d\nu_s \frac{\nu f_{\nu_s}^{\text{STAR}}}{4\gamma_e^2 \nu_s^2} h(\xi, b_\theta), \quad (24)$$

$$h(\xi, b_\theta) = 1 + \frac{\xi^2}{2(1-\xi)} - \frac{2\xi}{b_\theta(1-\xi)} + \frac{2\xi^2}{b_\theta^2(1-\xi)^2}, \quad (25)$$

where $f_{\nu_s}^{\text{STAR}} = \pi(R_\star/R_s)^2 2h\nu_s^3/c^2 [\exp(h\nu_s/kT_\star) - 1]$ is the flux density of the massive star photons, $\xi = h\nu/(\gamma_e m_e c^2)$, $b_\theta = 2(1 - \cos\theta_{\text{SC}})\gamma_e h\nu_s/(m_e c^2)$, $h\nu_s \ll h\nu \leq \gamma_e m_e c^2 b_\theta/(1 + b_\theta)$, θ_{SC} is the angle between the injecting photons and the scattered photons, and is varied along with the orbital phase.

4.3.4. γ -ray absorption

The intense radiation field provided by the companion star will absorb TeV photons through pair production. The differential absorption opacity for a γ -ray of energy E is given by (Gould & Schreder 1967; Dubus 2006b):

$$d\tau_{\gamma\gamma} = (1 - \cos\theta_{\gamma\gamma}) n_\epsilon \sigma_{\gamma\gamma} dl d\epsilon, \quad (26)$$

where $\theta_{\gamma\gamma}$ is the collision angle and n_ϵ is the photon density from the massive star. The $\gamma\gamma$ interaction cross section is given by (Gould & Schreder 1967):

$$\sigma_{\gamma\gamma} = \frac{\pi r_e^2}{2} (1 - \beta^2) \left[(3 - \beta^4) \ln \frac{1 + \beta}{1 - \beta} - 2\beta(2 - \beta^2) \right], \quad (27)$$

where $r_e = e^2/m_e c^2$ is the classical radius of electrons, and $\beta = \sqrt{1 - 1/s}$, $s = (\epsilon E/2m_e^2 c^4)(1 - \cos \theta_{\gamma\gamma})$. Absorption can only happen when $s > 1$ which give the threshold energy $\epsilon_{\min} = 2m_e^2 c^4/E(1 - \cos \theta_{\gamma\gamma})$ for interaction with a γ -ray photon of energy E . The total opacity for a γ -ray energy E can be obtained by integrating Eq. (26) over the travel distance and seed photon energy distribution. A more detailed description of γ -ray absorption in massive X-ray binaries can be found in Dubus (2006b).

The absorption spectra at inferior-conjunction and super-conjunction of the bow shock and the back shock are shown in Fig. 6. The orbital variation of γ -ray absorption at 1 TeV of the bow shock and the back shock in Fig. 7. We can see that the maximum absorption occur around 0.5 TeV at super-conjunction and shift to 1 TeV at inferior conjunction. The TeV photons produced at apex of the bow shock will suffer strong absorption due to a denser photon field. We assume that the TeV emissions of J1018.6 are mainly produced at the back shock region and ignore the contributions from the apex of the back shock.

4.3.5. Doppler boosting effect

According to the relativistic hydrodynamical simulations by Bogovalov et al.(2008), the shocked wind flows away from the apex to the tail which can reach highly relativistic speeds. It means that the high energy emissions from the shock tail should be beamed due to the Doppler boosting effect. The relativistic boost is given by:

$$D_{\text{obs}} = \frac{1}{\Gamma(1 - \beta \cos \theta_{\text{obs}})}, \quad (28)$$

with θ_{obs} being the angle between the direction of the flow and the line of sight, Γ being the Lorentz factor of the flow, and $\beta = \sqrt{1 - \Gamma^{-2}}$. The outgoing energy will be modified by $\nu = D_{\text{obs}} \nu'$ and the outgoing flux will be $F_{\nu} = D_{\text{obs}}^3 F'_{\nu'}$. When the line of sight is near the beaming direction, we will receive the Doppler-boosted radiations.

The relativistic aberration will also affect the inverse-Compton process (Dubus et al. 2010). The energy density from the star in the flow frame will be reduced by a factor of D_{\star}^2 , with the relativistic boost involved is given by:

$$D_{\star} = \frac{1}{\Gamma(1 - \beta \cos \theta_{\star})}, \quad (29)$$

θ_{\star} is the angle of the interaction photons and shock flows in the comoving frame.

Finally, the observed total flux densities from all the shock accelerated electrons at

frequency ν with can be calculated by

$$F_\nu = \frac{1}{4\pi d_L^2} \cdot D_{\text{obs}}^3 \cdot \int d\gamma_e N(\gamma_e) \cdot \left[P_\nu^{\text{SYN}}(\gamma_e) + \frac{dP_\nu^{\text{EIC}}(\gamma_e)}{d\Omega} \right] \cdot e^{-\tau_{\gamma\gamma}}. \quad (30)$$

5. Results

In this section, we present calculated results using the model described above and compare with observations. The detailed model parameters assumed in the model fitting are given in Table. 1. Since the system parameters are still unknown yet, we adopt a modest value of eccentricity and inclination with $e \simeq 0.35$ and $i \simeq 40^\circ$ which is similar to LS 5039. The observed fluxes are explained by a spin-down power $L_{\text{sd}} \sim 4 \times 10^{36} \text{ergs}^{-1}$. If the pulsar has a typical magnitude of the surface magnetic field $B_s \sim 10^{12} \text{G}$, the dipole radiation model predicts the pulsar spin-down predicts the rotation period of $P \sim 0.1\text{s}$. The Lorentz factor of the free pulsar wind is estimated by $\gamma_w \sim \sigma_L \gamma_L \sim 4 \times 10^5$. The best fit value of the injection spectral slope is $p = 1.5$, which is smaller than the prediction of standard Fermi first order shock acceleration model. This may hints that the electrons are accelerated via reconnection rather than Fermi process (Dubus et al. 2015).

In Fig. 8, we calculate the spectrum and compare with observations. We proposed that the X-ray emissions are mainly produced by the synchrotron radiation in the bow shock with $B \sim 5\text{G}$ at apex. The synchrotron cooling timescales in the bow shock for the particles with Lorentz factor $\gamma_e > 10^6$ is shorter than the IC cooling timescale in Klein-Nishina regime. The strong magnetic field and $\gamma\gamma$ absorption in this region will greatly reduce the TeV photons. We proposed that observed TeV γ -rays are mainly produced in the back shock region with a lower magnetic field of $B \sim 0.2\text{G}$, then the IC cooling dominates the synchrotron cooling for the electrons a Lorentz factor $\gamma_e \sim 10^7$, and hence the spectrum of IC emissions can extend to 10 TeV. It is shown that J1018.6 exhibits extremely powerful emissions at GeV band with a spectral shape consistent with a power-law and an exponential cut-off at energies of a few GeV (see Fig. 2) which is typical spectrum of γ -ray pulsars observed by *Fermi*/LAT. Here, we used the two-layer outer-gap model to fit the spectrum around GeV band. However, the flux variation along the orbital phase (see Fig. 1) indicates an additional component in GeV band. We leave this component discuss in Sec. 6.

In Fig. 9 and Fig. 10, we show our calculated light curves of X-ray and TeV γ -ray and compare them with observations. The sharp peak around phase 0 in X-ray and TeV light curves are mainly emitted in the tail of the bow shock due to the Doppler-boosting effect at inferior-conjunction. When the line of sight cross the beaming direction, we will receive the Doppler-boosting radiations. There is another broad sinusoidal modulation in X-ray light

curves while the modulation in TeV light curves are not so obvious as in X-ray. This broad peak can be produced by the apex of the bow shock due to variations of shock conditions. In previous model, it is usually believed that synchrotron originated X-ray emissions from the shock apex would show a peak around periastron due to a higher magnetic field. However, we show that it can be also possibly peak at the apastron. This is because in the shocked regions with strong magnetic fields and with denser seed photon fields, the radiative cooling timescales of electrons would be less than the dynamical timescales of these regions. For the energy loss of the electrons produced the X-ray emissions are mainly dominated by the IC cooling in Klein-Nishina regime, which means that $f_\nu \propto N_e \propto \tau_c \propto 1/u_* \propto R^2 \propto d^2$. The orbital distance varies with the orbital phase as sinusoidal function, which means that the X-ray flux will also vary in the same way. For the case of the back shock, the dynamical timescales will have a strong effect on the electron distribution, and the flux variation in the TeV light curves is not so obvious as in X-ray band. The IC cooling timescale at apastron is longer than that in periastron, which means that of electron remains much longer at higher energy. The hardening in the electron spectrum will compensates the effect of magnetic field, and thus show a flux maxima at apastron. As we can see that the cooling process of electrons will have a strong effect on the spectrum and light curves.

6. Conclusion and Discussion

In this paper, we discussed the mechanisms of high energy emissions from the gamma-ray binary 1FGL J1018.6-5856. We presented the data analysis using 7 yr data of *Fermi*/LAT. The GeV spectrum with a power-law and exponential cutoff at the LOW state can be well explained the two-layer outer-gap model of pulsar magnetosphere. For the spectrum at HIGH state, an enhancement at 0.1-10 GeV is seen exclusively. As seen in the γ -ray orbital light curves and phase-resolved spectrum at HIGH state, a pure magnetospheric emission can not explain the GeV emission of J1018.6 well since the magnetospheric emission is not expected to vary as the pulsar moves along its orbit in a binary. It is indicated that there should exist another additional components around GeV band emission.

Alternatively, the emission from the un-shocked pulsar wind up-scattering stellar photons can also contribute to the GeV emissions (e.g. Kapala et al. 2010). However, the Compton flux are expected to peak at super conjunction which is contrast to observations. Besides, an IC component around 1 GeV require the Lorentz factor of cold pulsar wind with $\gamma_w \approx 10^4$ which can not explain the spectrum in 10-100GeV. The inverse-Compton origin of this component seems can be ruled out. Kong et al. (2012) proposed that Doppler-boosting of synchrotron emission in the bow shock tail can explain the GeV flare and spectrum of

PSR B1259-63/LS 2883. However, a synchrotron spectrum cut off at the energy of 10 GeV will require a very small magnetic fields or a very high Lorentz factor of the bulk flow in the shock tail which seems inconsistent with observations. The variation of GeV light curves is difficult to be re-produced in via inverse-Compton scattering and it also does not favor the origin of Doppler boosting synchrotron radiation. A more detailed study of the *Fermi*/LAT data will provide us a better understanding of the GeV emissions.

We also investigated the emission mechanisms of X-ray and TeV γ -rays from J1018.6. In previous studies, it is generally believed that the observed non-thermal broad emissions from gamma-ray binaries are produced by the energetic particles at the shock apex close to the wind standoff region(e.g., Dubus 2006a). However, the intense stellar photon field at this location and corresponding high opacities owing to $\gamma\gamma$ absorption will reduce the TeV fluxes greatly. Furthermore, the phase-averaged γ -ray spectrum of J1018.6 extends up to ~ 20 TeV with $E_{\text{break}} \geq 10$ TeV, posing constraints on the magnetic field ($0.001 \leq B \leq 0.1$ G). Such a low magnetic field can not explain the observed X-ray flux. We proposed that the X-ray emissions are mainly produced by the synchrotron radiation in the shock apex with $B \sim 5$ G, while TeV γ -rays are mainly produced in the back shock region with a lower magnetic field of $B \sim 0.2$ G and small absorption of TeV photons. The emissions from the tail of the bow shock will also contribute to the observed flux when the star is behind the pulsar (at inferior conjunction). The sharp peaks around phase 0 in X-ray and TeV light curves are produced in this region due to the Doppler boosting effect while another broad peak around phase 0.35 are produced by the shock apex and back shock due to the shock variations.

In our model, we assume that the binary has a symmetrical shock geometry and simply divided the emission region in to 3 parts (see Fig. 4). However, the realistic shock geometries in gamma-ray binaries are much more complicated than our assumptions. According to the relativistic hydrodynamical simulations done by Bosch-Ramon et al. (2012, 2015), the orbital motion will also deflect the shock flows, and strong instabilities lead to the development of turbulence and wind mixing in the flows will also disrupted the shock structure and affect the shocked flow evolution. Detail numerical simulations on gamma-ray binaries will provide us more accurate estimates of shock regions, flow evolutions and emission models to explore the high-energy emissions from these systems.

When we have finished the draft of this paper, we noted that An & Romani (2017) appeared. According to their analysis, they find that the orbital modulation in the low-energy γ -ray band is similar to that in the X-ray band, suggesting a common spectral component. The orbital light curve above a GeV changes significantly, suggesting that the GeV emission contains significant flux from a pulsar magnetosphere. They find that a simple one-zone model is inadequate to explain the shock emission, but that beamed Synchrotron-self Comp-

ton radiation from adiabatically accelerated plasma in the shocked pulsar wind can reproduce the complex multiband light curves, including the variable X-ray spike coincident with the gamma-ray maximum. Although the physical situation we consider is similar, there are notable differences between our model and those of An & Romani (2017). Assuming that J1018.6 includes a pulsar, the GeV spectrum in the LOW state can be well explained by the two-layer outer gap model of pulsar magnetosphere. As for the shock radiations, we proposed that X-rays are mainly produced by the synchrotron radiation at the bow shock, and TeV γ -rays are mainly produced by the external inverse-Compton scattering at the back shock. The sharp peak in X-ray and TeV light curves are produced by in the shock tail due to the Doppler boosting effect at inferior-conjunction, while another broad sinusoidal modulations are produced by the apex of the bow shock and the back shock due to variations of shock conditions.

Table 1: Model parameters of 1FGL J1018.6-5856

System parameters		
eccentricity of orbit	e	0.35
inclination angle	i	45°
periastron angle	ω	90°
distance	d_L	5.4 kpc
orbital period	P_{orb}	16.54 days
Pulsar and pulsar wind		
spin down power	L_{sd}	$4 \times 10^{36} \text{erg s}^{-1}$
rotation period	P	0.05 s
surface magnetic field	B_s	$1 \times 10^{12} \text{G}$
Lorentz factor of free pulsar wind	γ_w	4×10^5
magnetization at the light cylinder	σ_L	5×10^3
magnetization evolution index	α	1.2
Star and stellar wind		
mass	M_\star	$31M_\odot$
radius	R_\star	$10R_\odot$
temperature	T_\star	38900K
mass loss rate	\dot{M}_w	$2 \times 10^{-8} M_\odot/\text{yr}$
velocity of stellar wind	v_w	$2 \times 10^8 \text{cm/s}$
Shocked region		
electron distribution index	p	1.5
acceleration efficiency	ζ	1.0
bulk Lorentz factor of the flow	Γ	2.0

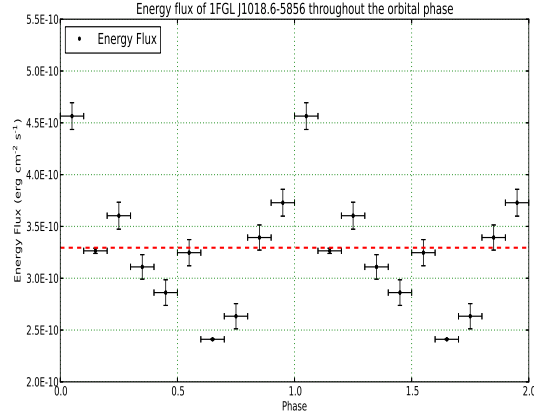


Fig. 1.— The orbital light curve of 1FGL J1018.6-5856 in 0.1 - 100 GeV obtained from binned likelihood analysis. The red dash-line indicates the mean energy flux.

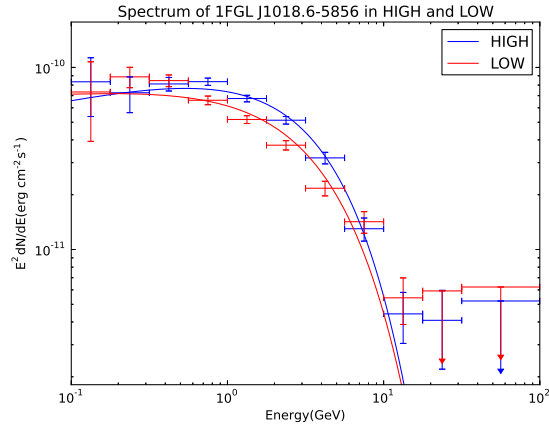


Fig. 2.— The orbital phase resolved spectra of 1FGL J1018.6-5856. Red and blue curves represent the LOW and HIGH states respectively.

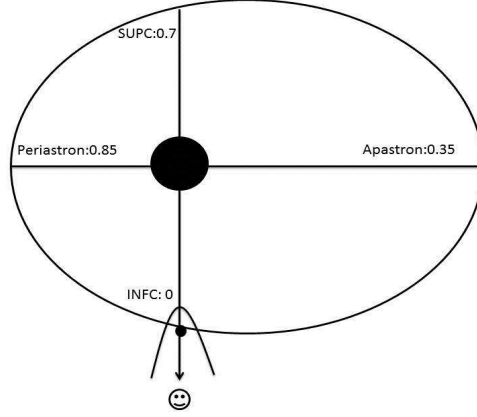


Fig. 3.— Schematic diagram of the orbital phases of J1018.6 in our model. The accurate determination of the orbital phase still need further observations.

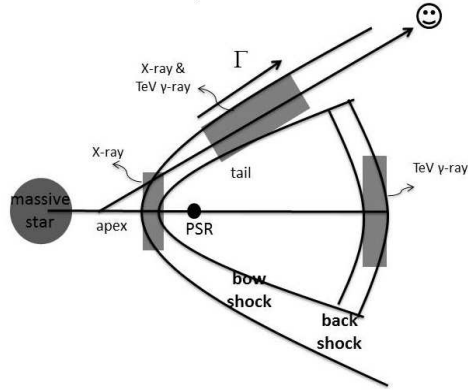


Fig. 4.— Geometry of the termination shock. The interaction between the pulsar wind and the stellar wind forms a bow shock with a hollow cone-like tail. As the particle flow propagating away from the apex, the bulk Lorentz will increase gradually to mild relativistic in the tail. The effect of orbital motion of the pulsar will also produce a termination shock in the opposite direction of the companion star (the back shock). The synchrotron radiation in the apex of the bow shock and the IC process in the back shock produce the X-rays and TeV γ -rays, respectively. The emissions from the tail of the bow shock will also contribute to the observed flux when the star is behind the pulsar (at inferior conjunction).

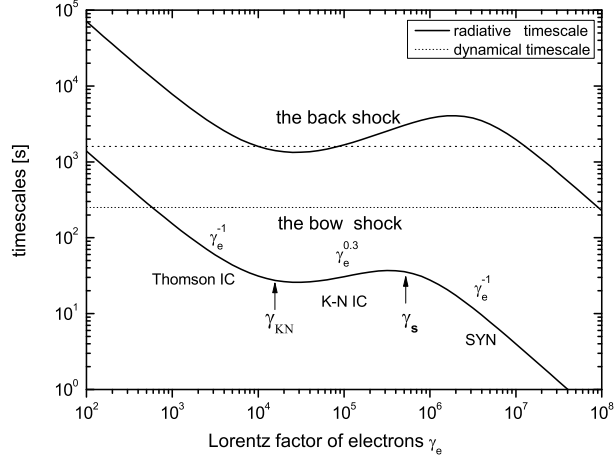


Fig. 5.— Cooling timescales with respect to the electron energies.

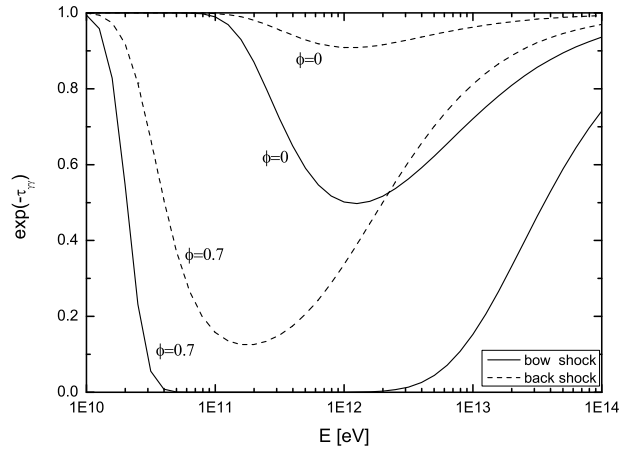


Fig. 6.— Spectrum of γ -ray absorption at inferior-conjunction ($\phi = 0$) and super-conjunction ($\phi = 0.7$) of the bow shock (solid lines) and the back shock (dashed lines).

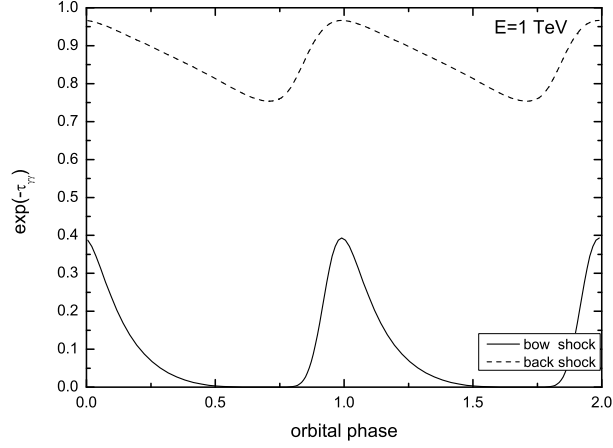


Fig. 7.— Orbital variation of absorption for $E=1$ TeV at the bow shock (solid lines) and the back shock (dashed lines).

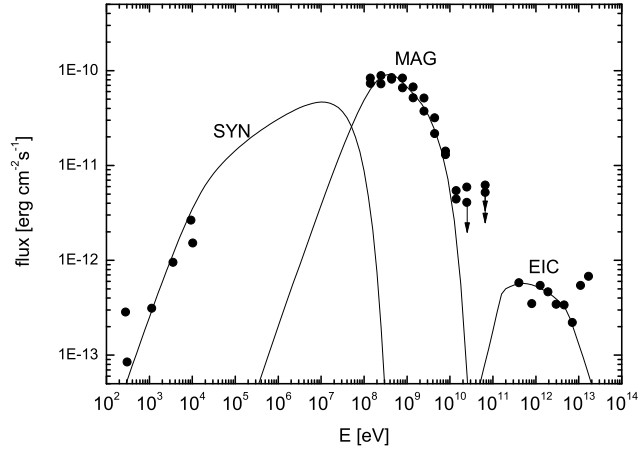


Fig. 8.— Calculated spectra as compared with observations. The X-ray data are taken from Dubus (2013) and the TeV data are taken from Abramowski et al. (2015) without error bars. The GeV data show the analysis result of the present work (Section 2). The solid lines show the results of the emission model discussed in Section 3 and Section 4. The X-ray emissions are mainly produced by the synchrotron radiation at the shock apex, and the TeV emissions are mainly produced by the inverse-Compton process at the back shock. The GeV emissions are mainly contributed by the outer-gap of the pulsar magnetosphere.

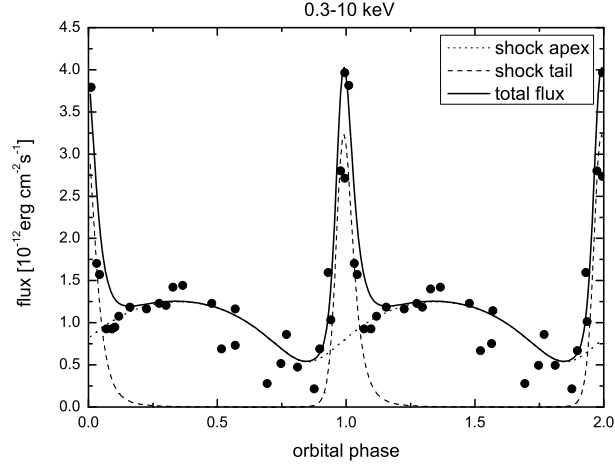


Fig. 9.— Calculated X-ray light curve as compared with observation. The X-ray data are taken from Ackerman et al. (2012) without error bars. The dotted line and the dashed line corresponding to the emission from the shock apex and the shock tail, respectively, and the solid line correspond to the total flux.

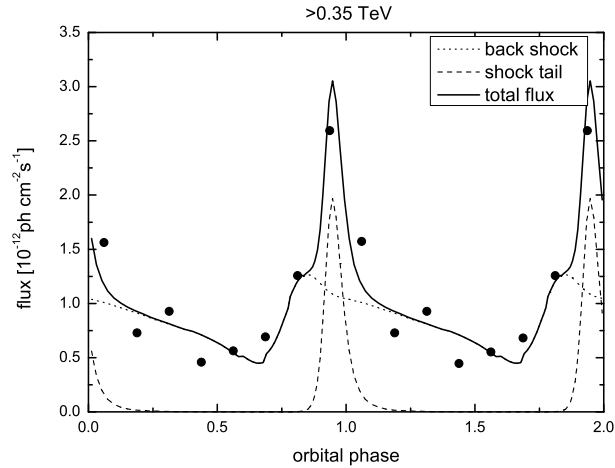


Fig. 10.— Calculated TeV light curve as compared with observation. The TeV data are taken from Abramowski et al. (2015) without error bars. The dotted line and the dashed line corresponding to the emission from the back shock and the shock tail, respectively, and the solid line correspond to the total flux.

REFERENCES

- Acero, F., Ackermann, M., Ajello, M., et al. 2015, *ApJS*, 218, 23
- Abramowski, A., Acero, F., et al. 2012, *A&A*, 541, A5
- Abramowski, A., Aharonian, F., et al. 2015, *A&A*, 577, A131
- Ackermann, M., Ajello, M., et al. 2012, *Science*, 335, 189
- Aharonian, F., Akhperjanian, A. G., Aye, K.-M., et al. 2005, *A&A*, 442, 1
- Aharonian, F., Akhperjanian, A. G., Bazer-Bachi, A. R., et al. 2006, *A&A*, 460, 743
- Aharonian, F. A., & Atoyan, A. M. 1981, *Ap&SS*, 79, 321
- Albert, J., Aliu, E., Anderhub, H., et al. 2006, *Science*, 312, 1771
- An, H., Dufour, F., Kaspi, V. M., & Harrison, F. A. 2013, *ApJ*, 775, 135
- An, H., Bellm, E., Bhalerao, V., et al. 2015, *ApJ*, 806, 166
- An, H., & Romani, R. W. 2017, arXiv:1703.04214
- Bogovalov, S. V., Khangulyan, D. V., Koldoba, A. V., Ustyugova, G. V., & Aharonian, F. A. 2008, *MNRAS*, 387, 63
- Bogovalov, S. V., Khangulyan, D., Koldoba, A. V., Ustyugova, G. V., & Aharonian, F. A. 2012, *MNRAS*, 419, 3426
- Bosch-Ramon, V., & Barkov, M. V. 2011, *A&A*, 535, A20
- Bosch-Ramon, V., Barkov, M. V., Khangulyan, D., & Perucho, M. 2012, *A&A*, 544, A59
- Bosch-Ramon, V., Barkov, M. V., & Perucho, M. 2015, *A&A*, 577, A89
- Cerutti, B., Dubus, G., & Henri, G. 2008, *A&A*, 488, 37
- Chai, Y., Cheng, K. S., & Takata, J. 2016, *JASS*, 33, 75
- Cheng, K. S., Ho, C., & Ruderman, M. 1986a, *ApJ*, 300, 500
- Cheng, K. S., Ho, C., & Ruderman, M. 1986b, *ApJ*, 300, 522
- Corbet, R. H. D., Chomiuk, L., Coe, M. J., et al. 2016, *ApJ*, 829, 105
- Dubus, G. 2006a, *A&A*, 456, 801

- Dubus, G. 2006b, *A&A*, 451, 9
- Dubus, G., Cerutti, B., & Henri, G. 2008, *A&A*, 477, 691
- Dubus, G., Cerutti, B., & Henri, G. 2010, *A&A*, 516, A18
- Dubus, G., Lamberts, A., & Fromang, S. 2015, *A&A*, 581, A27
- Dubus, G. 2013, *A&A Rev.*, 21, 64
- Eichler, D., & Usov, V. 1993, *ApJ*, 402, 271
- Ginzburg, V. L., & Syrovatskii, S. I. 1964, *The Origin of Cosmic Rays*, New York: Macmillan, 1964,
- Gould, R. J., & Schröder, G. P. 1967, *Physical Review*, 155, 1404
- Hinton, J. A., Skilton, J. L., Funk, S., et al. 2009, *ApJ*, 690, L101
- Hobbs, G. B., Edwards, R. T., & Manchester, R. N. 2006, *MNRAS*, 369, 655
- Kapala, M., Bulik, T., Rudak, B., Dubus, G., & Lyczek, M. 2010, *25th Texas Symposium on Relativistic Astrophysics*, 193
- Kennel, C. F., & Coroniti, F. V. 1984a, *ApJ*, 283, 694
- Kennel, C. F., & Coroniti, F. V. 1984b, *ApJ*, 283, 710
- Kirk, J. G., Ball, L., & Skjæraasen, O. 1999, *Astroparticle Physics*, 10, 31
- Kong, S. W., Cheng, K. S., & Huang, Y. F. 2012, *ApJ*, 753, 127
- Kong, S. W., Yu, Y. W., Huang, Y. F., & Cheng, K. S. 2011, *MNRAS*, 416, 1067
- Lyne, A. G., Stappers, B. W., Keith, M. J., et al. 2015, *MNRAS*, 451, 581
- Moderski, R., Sikora, M., Coppi, P. S., & Aharonian, F. 2005, *MNRAS*, 363, 954
- Ray, P. S., Kerr, M., Parent, D., et al. 2011, *ApJS*, 194, 17
- Rybicki, G. B., & Lightman, A. P. 1979, New York, Wiley-Interscience, 1979. 393 p.,
- Sierpowska-Bartosik, A., & Torres, D. F. 2007, *ApJ*, 671, L145
- Strader, J., Chomiuk, L., Cheung, C. C., Salinas, R., & Peacock, M. 2015, *ApJ*, 813, L26
- Takata, J., Leung, G. C. K., Tam, P. H. T., et al. 2014, *ApJ*, 790, 18

- Takata, J., Ng, C. W., & Cheng, K. S., 2016, MNRAS, 455, 4249T
- Tavani, M., & Arons, J. 1997, ApJ, 477, 439
- Torres, D. F. 2011, Astrophysics and Space Science Proceedings, 21, 531
- Wang, Y., Takata, J., & Cheng, K. S. 2010, ApJ, 720, 178
- Wang, Y., Takata, J., & Cheng, K. S. 2011, MNRAS, 414, 2664
- Wex, N. 1998, MNRAS, 298, 67
- Zabalza, V., Bosch-Ramon, V., Aharonian, F., & Khangulyan, D. 2013, A&A, 551, A17